

JGR Solid Earth

RESEARCH ARTICLE

10.1029/2020JB019998

Key Points:

- A 3-D sedimentary structure of southeastern Australia is built by jointly inverting passive seismic datasets
- The sediments in the Murray basin are less consolidated compared with those in Sydney-Gunnedah-Bowen Basin
- Two low-velocity zones are imaged in the upper and middle crystalline crust under Flinders Ranges and Begargo Hill volcanic zone

Supporting Information:

- Supporting Information S1

Correspondence to:

F. Niu,
niu@rice.edu

Citation:

Li, G., Yang, Y., Niu, F., & Chen, M. (2021). 3-D sedimentary structures beneath southeastern Australia constrained by passive seismic array data. *Journal of Geophysical Research: Solid Earth*, 126, e2020JB019998. <https://doi.org/10.1029/2020JB019998>

Received 16 APR 2020
 Accepted 23 NOV 2020

3-D Sedimentary Structures Beneath Southeastern Australia Constrained by Passive Seismic Array Data

Guoliang Li^{1,2} , Yingjie Yang² , Fenglin Niu^{1,3} , and Min Chen^{4,5} 

¹State Key Laboratory of Petroleum Resource and Prospecting, Unconventional Petroleum Research Institute, China University of Petroleum at Beijing, Beijing, China, ²Department of Earth and Planetary Science, Australian Research Council Centre of Excellence for Core to Crust Fluid Systems and GEMOC, Macquarie University, North Ryde, NSW, Australia, ³Department of Earth, Environmental and Planetary Sciences, Rice University, Houston, TX, USA, ⁴Department of Computational Mathematics, Science and Engineering, Michigan State University, East Lansing, MI, USA, ⁵Department of Earth and Environmental Sciences, Michigan State University, East Lansing, MI, USA

Abstract A high-resolution sedimentary map of southeastern Australia is of great importance to explore natural resources as well as to evaluate seismic hazards. In this study, we build a 3-D Vs model of the upper crust beneath southeastern Australia by jointly inverting Rayleigh wave phase velocity, ellipticity, and teleseismic P-coda waves. At depths less than 3 km, sedimentary basins are revealed as prominent low-velocity anomalies. The average sediment depth in the Murray Basin is ~713 m with the maximum depth reaching 1,500 m, while, in the Sydney-Gunnedah-Bowen Basin (SGBB), the average sediment depth is 600 m with a maximum depth of ~3,000 m. Vs of the sedimentary layer in the Murray Basin is lower than that in the SGBB, suggesting that the sediments in the Murray Basin are less consolidated compared with those in the SGBB. The unconsolidated sediments make the Murray Basin more vulnerable to seismic hazards. In the upper and middle crystalline crust, we image two low-velocity zones: one beneath the Adelaide Fold Belt and the other beneath the Begargo Hill volcanic zone. The low-velocity zone beneath the Adelaide Fold Belt is likely caused by high temperature and/or a weak granitic composition, which lead to the concentration of intraplate seismic activities in this area. The low-velocity zone beneath the Begargo Hill Volcanic zone indicates that there exists magma in the upper to middle crust or the temperature there is still very high after the latest eruption.

1. Introduction

The sedimentary basins in southeastern Australia host some important resources, and knowledge of seismic structures of sediment is essential for better resource exploration. For example, the Sydney Basin contains a large amount of coal and natural gas resources and has been the focus of exploration for decades. Besides, the Gawler Craton in southern Australia is home to the Olympic Dam deposits, containing ~40% percent of the world's known U resources as well as other world-class resources of Cu and Au (Hand et al., 2007). Mapping the seismic structure of the upper crust beneath southeastern Australia is of great interest in exploring and evaluating those natural resources. Although it is generally regarded as a seismically inert continent, Australia did occasionally experience moderate earthquakes with magnitudes greater than 5, which incurred significant damages and casualties. For example, the Newcastle earthquake in 1989 killed more than 10 people and resulted in \$4 billion of property damages (Denham, 1992). Although to date, we still cannot precisely predict when and where earthquakes occur, we can model the ground shaking induced by earthquakes and calculate the site amplification coefficients for earthquake hazard areas, which is fundamental to alleviate earthquake hazards. A reliable shear wave velocity (Vs) model of sedimentary basins is the prerequisite for modeling ground shaking and calculating amplification.

A number of seismic studies have been carried out to image the crustal and upper mantle structures in southeastern Australia (e.g., Jiang et al., 2016; Pilia et al., 2015; Rawlinson et al., 2016; Saygin & Kennett, 2010; Young et al., 2013). Most of these previous studies use dispersion curves of surface waves to constrain the crustal structures. However, the dispersion curves of surface waves have limited sensitivities to shallow structures, making it hard to accurately resolve the sedimentary structures at the top of the crust. Reflection seismology using active seismic data is capable of imaging detailed structures of sedimentary basins. However, due to the high cost of field operation, reflection surveys have only been carried

out along a few limited transects (Kennett et al., 2016), leaving most of southeastern Australia unexplored. Gravity modeling can also be used to map 3-D regional shallow structure (e.g., Danis et al., 2011; Krassay et al., 2009). However, gravity modeling of sedimentary basins is highly dependent on initial density values used in the modeling, which cannot be accurately constrained. Without proper density constraints from boreholes and seismic profiles, the uncertainties of the modeled sedimentary basement can be up to 1 km (Danis et al., 2011).

Compared with active seismic surveys and borehole core measurements, passive seismic data are more affordable and more convenient to collect. A recent study by Li et al. (2019) demonstrates that jointly inverting teleseismic P-coda waveforms, Rayleigh wave phase velocity and ellipticity can better constrain velocities and velocity discontinuities of sedimentary basins. In this study, we adopt the method developed by Li et al. (2019) and use the passive seismic datasets recorded by the Wombat array to construct the upper crustal structure of southeast Australia. The 3-D upper crustal V_s model is fundamental to improve the exploration of resources and also contribute to alleviating earthquake hazards in southeastern Australia.

2. Geological Settings

Our study region covers the Gawler Craton, the Delamerian Orogen (including the Adelaide Fold Belt), the Curnamona Province, Lachlan Orogen and the New England Orogen as shown in Figure 1 from west to east. Among them, the Gawler Craton is the oldest geological unit, which was formed from the late Archean to the early Mesoproterozoic, in total spanning about 1 billion years (Hand et al., 2007; Payne et al., 2008). To the east of the Gawler Craton is the Delamerian Orogen (including the Adelaide Fold Belt), which separates the Australia Precambrian cratons from the younger Paleozoic to Mesozoic orogens in eastern Australia (Jenkins et al., 1992; Miller et al., 2005). The circular-shaped Curnamona Province, a Paleo- to Mesoproterozoic crustal province, lies to the east of Adelaide rift complex. The lithological similarity between the eastern margin of the Gawler and the southern part of the Curnamona Province suggests that the Curnamona province and Gawler Craton were once part of the same contiguous crust prior to the Neoproterozoic but are now separated by the Adelaide rift complex (Conor & Preiss, 2008; Wade et al., 2012; Wingate et al., 1998). To the east of the Delamerian Orogen is the Lachlan Orogen which covers most of the southeastern portion of Australia, belonging to part of a Paleozoic convergent system that stretched around the Gondwana supercontinent (Foster & Gray, 2000). The New England Orogen is located in the easternmost of the study area and is the youngest orogen in the Tasmanides (Glen, 2013; Jessop et al., 2019). In addition, in our study area, two main basin systems are superimposed on those orogens, that is, the Murray Basin overlaying the Adelaide Fold Belt and the Lachlan Orogen, and the Sydney-Gunnedah-Bowen Basin (SGBB) system on top of the Lachlan Orogen (Figure 1b).

3. Data and Methods

3.1. Wombat Array

The passive seismic data used in this study are from the Wombat Array, which comprises a multitude of small subarrays sequentially deployed from 1999 to 2012 and their digital objective identifier (DOI) are listed in the Table S1 in the supporting material. The deployment durations of those subarrays varied from 4 to 12 months and the spacing among these stations is around 50 km. The Wombat Array consists of a total of over 400 narrow band seismic stations. As some of the early stations are mounted with single-component seismometers, we only collect continuous seismic data from a total of 294 stations with three-component (3-C) seismometers, including subarrays of SEAL2, SEAL3, GW, CU, EAL1, EAL2, and EAL3 as shown in Figure 1a.

3.2. Extracting Rayleigh Wave Phase Velocities from Ambient Noise Data

To extract surface wave phase velocities from ambient noise, we adopt the data processing procedures (Bensen et al., 2007; Li et al., 2016; Lin et al., 2012, 2014). Here, we only briefly describe these procedures.

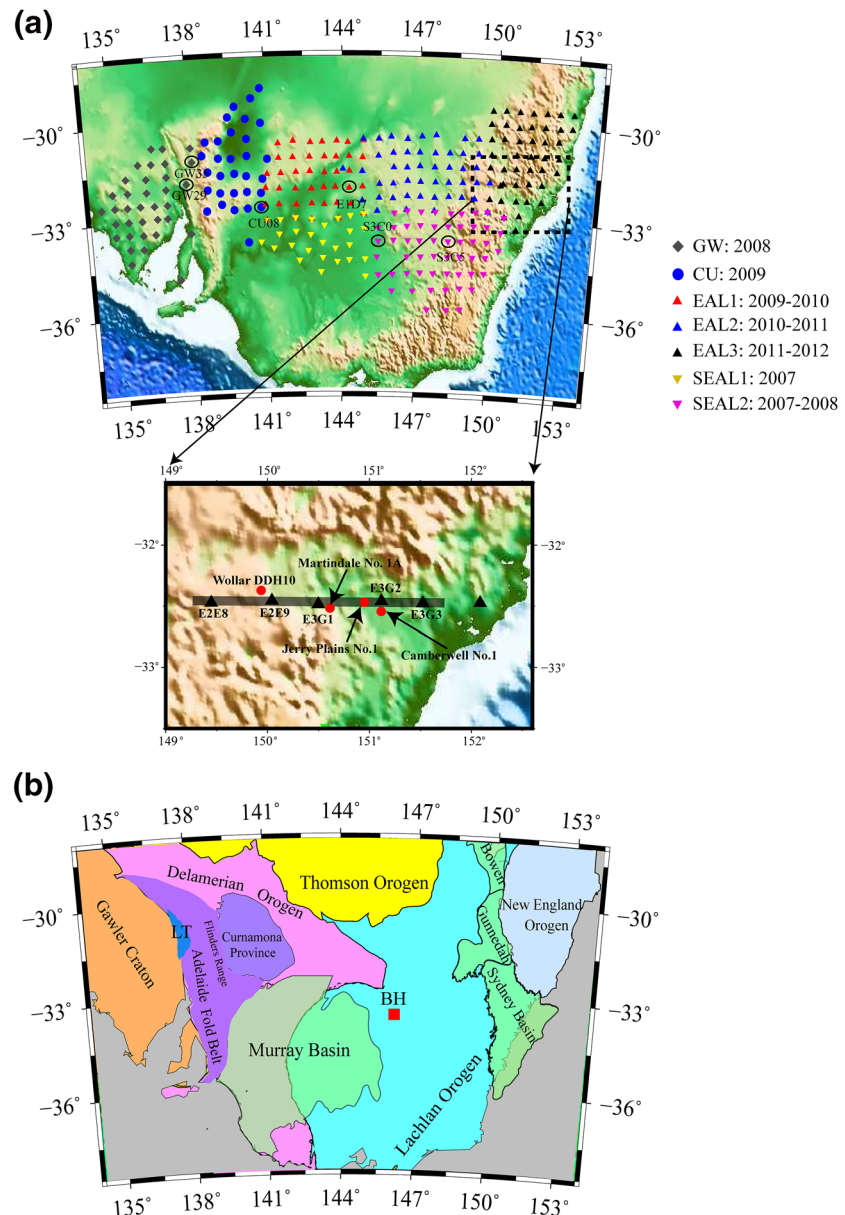


Figure 1. (a) Locations of seven subarrays of Wombat Array used in this study. The subarrays are GW, CU, EAL1, EAL2, EAL3, SEAL2, and SEAL3, which were deployed in different time periods. Several stations mentioned in the following sections are denoted. The dashed rectangle outlines the area where the four boreholes (red dots) are located as shown in the inset. The thick gray line in the inset delineates the locations of the profile shown in Figure 10. (b) Simplified geological map of southeastern Australia showing the main tectonic units. The Murray Basin and the Sydney-Gunnedah-Bowen Basin (SGBB) are superimposed on geological structures as green shadows. The Begargo Hill volcanic zone, abbreviated as BH, is marked as the small red rectangle. The Lake Torrens, abbreviated as LT, is filled in blue.

We collect 3-C continuous seismic data from 294 stations over their whole deployment durations. Then, we cut the continuous data into daily segments and remove the trends, the means, and the instrument responses from all the seismograms. Afterward, we bandpass filter all the daily seismograms in the period range of 1–20 s period and decimate them to five samples per second. Finally, we apply the same temporal normalization in time domain using a running-absolute-mean normalization method and same spectral whitening to all three components to ensure the relative amplitudes among the three components are retained (Lin et al., 2014). After the preprocessing procedures for each station, we perform cross-correlations between all

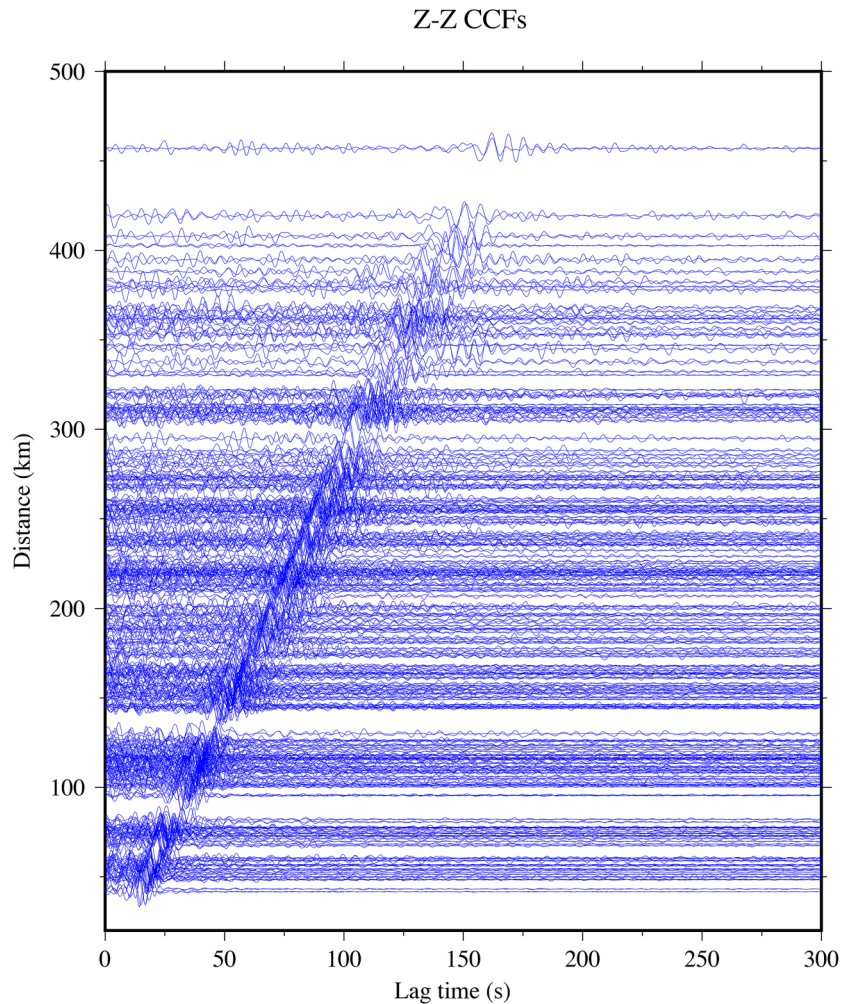


Figure 2. Symmetrical components of Z-Z CCFs. These CCFs are randomly selected from the whole data set of our Z-Z CCFs. CCF, cross-correlation function.

the three components for all available station pairs among the 294 stations. Thus, for each station pair, we have nine cross-correlation functions (CCFs) (Z-Z, Z-E, Z-E, N-Z, N-N, N-E, E-Z, E-N, E-E).

We obtain Rayleigh wave phase velocity measurements from Z-Z CCFs. To improve the signal-to-noise ratios (SNRs) of the Rayleigh wave signals, we first linearly stack daily Z-Z CCFs over a continuous span of 5 days without any overlap in time between individual 5-day spans. Then, we further stack all the 5-days stacks to obtain the final stacked Z-Z CCFs using a time-frequency phase weight stacking (tf-PWS) method developed by Li et al. (2017). Li et al. (2017) have demonstrated that the tf-PWS method can significantly improve the SNRs of surface wave signals without distorting dispersion measurements from resulting stacked CCFs. More details about this stacking method are described in length in Li et al. (2017).

To further increase the SNRs of CCFs, we cut and stack the positive and negative lags of each CCF to obtain the so-called symmetrical component of CCFs. Some examples of Z-Z CCFs are plotted in Figure 2, which shows clear Rayleigh wave arrivals with a move-out velocity of 2.70 km/s. We then measure phase velocity dispersion curves from the symmetrical components of the CCFs for all station pairs using an automatic frequency-time analysis (FTAN) (e.g. Dziewonski et al. 1969; Herrin & Goforth, 1977; Levshin & Ritzwoller, 2001). Having the phase velocity measurements among all the 294 stations, we only select those measurements with SNR larger than 10 and interstation distances longer than two wavelengths for tomography. We adopt the Fast Marching Surface wave Tomography method (Kennett et al., 1988; Rawlinson &

Sambridge, 2004a, 2004b) to perform the tomography using all the selected interstation dispersion curves of Rayleigh waves from the Z-Z CCFs at periods of 3–15 s.

3.3. Estimating Rayleigh Wave Z/H Ratio from Ambient Noise

As described in the preceding subsection, we apply the same temporal normalization and spectral whitening to the three components of each individual station. Therefore, the relative amplitude information among the three components is preserved for each station. Because the tf-PWS method does not preserve amplitude information in stacking, we instead linearly stack the nine daily CCFs for each station pairs in order to measure the Rayleigh waves Z/H ratios. After obtaining the stacks of all the CCFs, we separate the positive and negative parts of each CCFs and mark those single-side NCFs with different names as described in the following paragraph. Then we rotate those single-side CCFs to obtain Z-R R-Z and R-R CCFs following the rotation matrix defined in Li et al. (2016).

To measure the Z/H ratio from the stacked Z-Z, Z-R, R-Z, and R-R CCFs, we employ the methods of Lin et al. (2014) and Li et al. (2016). For one station pair of A and B, the Z/H ratio for a given period at station A can be estimated from:

$$\begin{aligned} ZH(T) &= \frac{Z_B Z_A}{Z_B R_A} = \frac{R_B Z_A}{R_B R_A} = \frac{Z_A Z_B}{R_A Z_B} = \frac{Z_A R_B}{R_A R_B} \\ &= \frac{Z_{\text{stack}}}{R_{\text{stack}}} \end{aligned} \quad (1)$$

where,

$$\begin{aligned} Z_{\text{stack}} &= Z_B Z_A + iH[R_B Z_A] + Z_A Z_B + H[Z_A R_B] \\ R_{\text{stack}} &= H[Z_B R_A] + R_B R_A + iH[R_A Z_B] + R_A R_B \end{aligned} \quad (2)$$

here, the first and second letters represent the components of the virtual source station and the receiver station, respectively; and the first and second subscripts represent the virtual source station and the receiver station, respectively. For example, $Z_A R_B$ denotes the radial component of a Rayleigh wave recorded at station B from a vertical impulse source at station A, while $R_B Z_A$ represent the vertical component of a Rayleigh wave recorded at station A from a horizontal impulse source at station B. $Z_A R_B$ and $R_B Z_A$ are the single-side NCFs that are produced from two-side NCFs. As it is well known, there is a 90° phase difference between the horizontal component (R) and vertical component (Z) of Rayleigh waves. After cross-correlation operation, Rayleigh waves in Z-Z and R-R CCFs are in phase. However, phases of Rayleigh waves in Z-R and R-Z CCFs are respectively advanced and delayed by 90°. To measure Z/H ration, we first need to calibrate the phases of different CCFs to make sure the Rayleigh waves in all CCFs are in phase. To do that, we apply Hilbert transform to ZR or 90°-phase advanced transform to RZ in order to keep them in phase with ZZ (or RR). In Equation 2, the operation $H[]$ and $iH[]$ result in 90° phase delay or phase advance for a given waveform. After the phase calibration, the phases of all used CCFs as well as Z_{stack} and R_{stack} , are in phase. For a given period, we narrowly filter the stacked vertical (Z_{stack}) and radial (R_{stack}) components using bandpass filters centered at the periods of interest. We then compute the zero-lag cross-correlation coefficient of the Z_{stack} and R_{stack} . The measurement is discarded if that coefficient is less than 0.8. Finally, the envelope functions of the vertically and radially stacked components are calculated, and the maximum values of the envelope functions are used to estimate the Z/H ratio. The final Z/H ratio for a station is the average of Z/H ratio measures from CCFs with all other stations.

An example of estimated Z/H ratio curves for station pair S3C0 and S3C5 are shown in Figures 3a and 3b. Station S3C0 was deployed in the rim of Murray Basin, while station S3C5 was placed in the Lachlan Orogen. Therefore, the estimated Z/H values at all the period band of station S3C0 are less than those of station S3C5. Furthermore, the narrowly bandpass filtered (0.11–0.14 Hz) Z-Z, Z-R, R-Z, R-R CCFs of the two stations are also illustrated in Figures 3c and 3d. From the bandpass filtered CCFs, phase differences

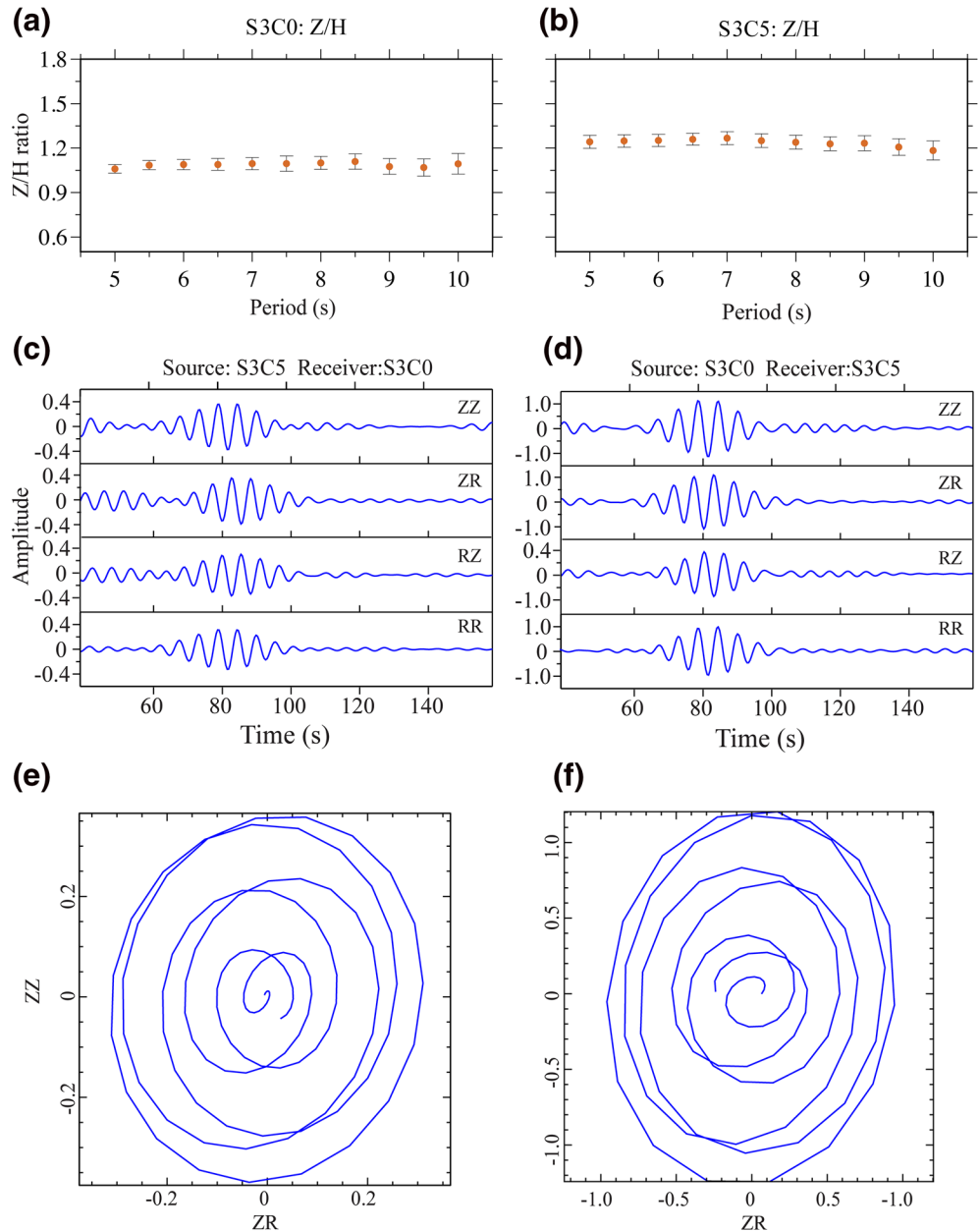


Figure 3. (a) and (b) Measured Z/H ratios and corresponding standard deviations, marked by the error bars for one station pair: S3C0 and S3C5. The locations of these two stations are marked in Figure 1a. (c) Narrowly bandpass filtered Z-Z, Z-R, R-Z, R-R CCFs at 0.11–0.14 Hz with station S3C5 acting as a virtual source and station S3C0 as a receiver. Note the phase differences between the four CCFs. (d) same as (c), but for CCFs with station S3C0 acting as a virtual source and station S3C5 as a receiver. (e) and (f) show the particle motions of Rayleigh waves from Z-Z and Z-R CCFs for station S3C0 and S3C5 respectively. CCF, cross-correlation function.

between different components are noticeable. The corresponding particle motions for the bandpassed Z-Z and Z-R CCFs are also plotted in Figures 3e and 3f, respectively.

3.4. Teleseismic Body Waveforms

When a teleseismic P wave is incident at the base of a sedimentary basin, some part of P wave energy is converted to S wave. The converted S wave reverberates within the sedimentary layer with nearly vertical ray paths because of the very low S wave velocity in the sedimentary layer compared to the basement. The

converted S wave, which is mostly recorded in the horizontal component, interferes with the direct P wave and causes a delay in P arrival time in the horizontal component as compared to the vertical component (Bao & Niu, 2017; Yang & Niu, 2019). This time delay between the vertical and horizontal components can provide constraints on the sedimentary structure and basement.

Here we adopt the cross-convolution method (Bodin et al., 2014; Menke & Levin, 2003) to incorporate the teleseismic waveforms in the joint inversion:

$$\begin{aligned} V_{\text{obs}}(t) * h_{\text{syn}}(t, m) &= s(t) * v(t) * I(t) * h_{\text{syn}}(t, m) \\ H_{\text{obs}}(t) * v_{\text{syn}}(t, m) &= s(t) * h(t) * I(t) * v_{\text{syn}}(t, m) \end{aligned} \quad (3)$$

where $V_{\text{obs}}(t)$ and $H_{\text{obs}}(t)$ represent observed vertical and radial waveforms of P and converted S wave recorded at a given station. $I(t)$ and $s(t)$ represent the instrument response of the seismometer and the source time function of the teleseismic event, respectively. * indicates the operation of convolution. Additionally, $v(t)$ and $h(t)$ are the vertical and horizontal component of Green's functions of the sedimentary layer, while $v_{\text{syn}}(t, m)$ and $h_{\text{syn}}(t, m)$ are the synthetic vertical and radial Green's functions of a trial model m . If the trial model m is the same as the true model, then $v_{\text{syn}}(t, m) = v(t)$ and $h_{\text{syn}}(t, m) = h(t)$.

Because the Green's functions of the shallow structure ($h_{\text{syn}}(t, m)$ and $v_{\text{syn}}(t, m)$) are almost independent from epicentral distances (Li et al., 2019) in the distance range of 30°–90° and the convolution operator is linear, we stack the recorded teleseismic waveforms from different teleseismic events by aligning waveforms according to their maximum vertical amplitude in order to suppress the random noise and to reduce the number of event waveforms to be fitted. Before stacking, for each event, the vertical and radial records are first normalized by the maximum amplitude of the vertical components and the negative polarity is reverse to positive polarity. Therefore, Equation 3 can be rewritten as:

$$\begin{aligned} h_{\text{syn}}(t, m) * \frac{1}{N} \sum_{i=1}^N V_{\text{obs}}^i(t) &= v(t) * I(t) * h_{\text{syn}}(t, m) * \frac{1}{N} \sum_{i=1}^N s_i(t) \\ v_{\text{syn}}(t, m) * \frac{1}{N} \sum_{i=1}^N H_{\text{obs}}^i(t) &= h(t) * I(t) * v_{\text{syn}}(t, m) * \frac{1}{N} \sum_{i=1}^N s_i(t) \end{aligned} \quad (4)$$

here N is the total number of teleseismic events. We select teleseismic events with amplitude magnitudes greater than 5.5 and with the epicentral distances ranging between 30° and 90° and then stack the recorded body wave waveforms. We only stack those vertical and radial components with an SNR > 10. Here, the SNR is defined as the maximum amplitude of the P wave to the root mean square of noise data within a window starting at 70 s before the arrival time of the P wave and ending at 20 s before the arrival time of the P wave. By stacking via this way, the signals are stacked constructively at the moment of maximum vertical amplitude. Figure 4 illustrates two examples of the stacking procedures for station CU08 and E1D7. Station CU08 was deployed inside the Murray Basin and the stacked horizontal waveform shows prominent sedimentary reverberations in a time window of 0–4 s, and also there is a clear delay of the horizontal first arrival relative to the first arrival of the vertical component; whereas, station E1D7 was located in the Lachlan Orogen and the stacked horizontal waveform is rather simple and there is no delay between vertical and horizontal components.

3.5. The Joint Inversion

Rayleigh wave Z/H ratio helps constrain the shallow Vs structure in the joint inversion, and phase velocity dispersion curves mainly help constrain the deep Vs structure. Since the longest period of the phase velocity we extract from CCFs is 15 s, the maximum depth of structures Rayleigh wave can resolve is ~20 km based on the phase velocity sensitivity kernels in Figure 5, which are calculated from the Preliminary reference model (Dziewonski & Anderson 1981). Body waveforms are sensitive to velocity discontinuities. Here, we adopt a joint Bayesian Monte Carlo nonlinear inversion method (e.g., Afonso et al., 2013; Li et al., 2019; Shen and Ritzwoller 2016) to invert the three types of data for upper crustal structures in southeastern Australia. We briefly describe the joint method below.

The likelihood function in the joint inversion is defined as the following equation:

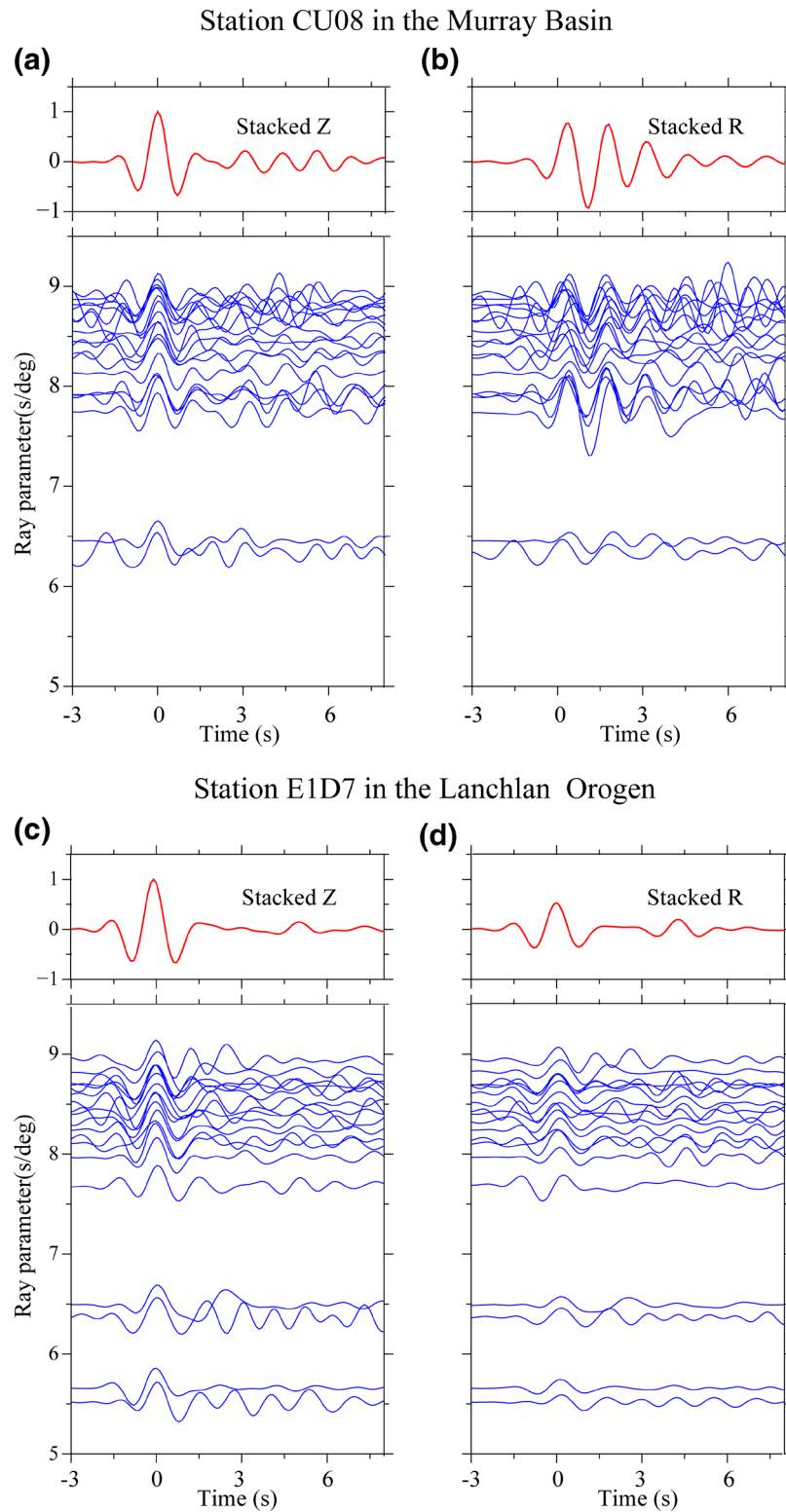


Figure 4. Vertical- (Z) and radial-component (R) waveforms from teleseismic events recorded at station CU08 (a)–(b) and E1D7 (c)–(d). The vertical components are plotted in the left panels and the radial components in the right. In each panel, the top diagram is the waveform stacked from the individual ones plotted at the bottom diagram. The individual waveforms are filtered at a frequency band of 0.05–0.5 Hz. Individual waveforms are aligned according to their maximum vertical amplitude. Note the strong reverberation signals in the radial-component waveforms recorded at station CU08 located in the Murray Basin.

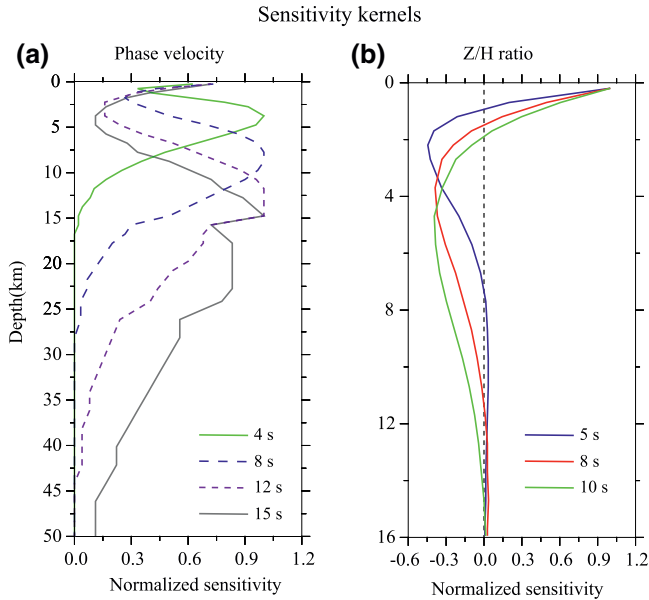


Figure 5. Sensitivity kernels calculated from the preliminary reference model. (a) Sensitivity kernels of Rayleigh wave phase velocities at periods of 4, 8, 12, and 15 s. (b) Sensitivity kernels of Raleigh wave Z/H ratio at periods of 5, 8, and 10 s.

$$p(d_{\text{obs}} | m) = \frac{1}{\prod_{i=1}^3 (\sqrt{2\pi}\sigma_i)} e^{-\frac{1}{2}\chi_{\text{joint}}(m)} \quad (5)$$

where

$$\begin{aligned} \chi_{\text{joint}}(m) &= \chi_{PH} + \chi_{ZH} + \chi_{BH} \\ &= \frac{1}{N} \sum_{i=1}^N \frac{[\text{PH}_i(m) - \text{PH}_i^{\text{obs}}]^2}{\sigma_1^2} + \frac{1}{M} \sum_{j=1}^M \frac{[\text{ZH}_j(m) - \text{ZH}_j^{\text{obs}}]^2}{\sigma_2^2} + \frac{\phi(m)}{\sigma_3^2} \end{aligned} \quad (6)$$

here, PH_i^{obs} and ZH_j^{obs} represent the observed phase velocity and Z/H ratio at certain periods, while $\text{PH}_i(m)$ and $\text{ZH}_j(m)$ are the calculated phase velocity and Z/H ratio at the i th and j th periods for a candidate model generated by the Monte Carlo method. N and M are the numbers of periods used in the inversion. $\phi(m)$ is the misfit function of the teleseismic events and is defined as:

$$\phi(m) = 1 - \frac{\int_{T_1}^{T_2} \{V_{\text{obs}}(t) * h_{\text{syn}}(t, m)\} \cdot \{H_{\text{obs}}(t) * v_{\text{syn}}(t, m)\} dt}{\sqrt{\int_{T_1}^{T_2} |V_{\text{obs}}(t) * h_{\text{syn}}(t, m)|^2 dt} \cdot \sqrt{\int_{T_1}^{T_2} |H_{\text{obs}}(t) * v_{\text{syn}}(t, m)|^2 dt}} \quad (7)$$

here, T_1 and T_2 represent the starting and end time of a time window that contains the direct P wave and sediment reverberations. The time window is set to 3 s before and 7 s after the maximum P on the vertical amplitude. The uncertainties (σ_1 , σ_2 , and σ_3) of the three kinds of datasets are usually difficult to determine and we here treat them as unknown parameters, which are also inverted during the joint inversion. For a given trial model, we use the method of Computer Programs in Seismology (Herrmann, 2013) to compute the dispersion curves, and use the Thomson-Haskell propagator matrix method (Haskell, 1962; Thomson, 1950) to calculate synthetic P-wave Green's functions.

We parametrize the 1-D velocity model beneath each station in three layers, that is, the sedimentary layer, the crystalline crust, and the upper mantle. In the sedimentary layer, the velocity structure is determined by three variables, which are V_s at the top and the bottom and sediment thickness. In our study, V_s in the sedimentary layer is assumed to increase linearly, which is the first-order approximation of the actually complex sedimentary structure. V_p in the sedimentary layer is related to V_s using the empirical function proposed by the Castagna et al. (1985):

$$V_p = 1.16V_s + 1.36. \quad (8)$$

And the density of sediments is further scaled by the Gardner's Law (Gardner et al., 1974)

$$\rho = 1.74V_p^{1/4}. \quad (9)$$

In the crystalline crust, V_s variation over depth is represented by the combination of four cubic B-splines, and the Moho depth is also treated as a variable. Therefore, a total of five parameters are employed to represent the crystalline crust. As the longest period of phase velocity measurement is 15 s, our data are insensitive to the mantle part. Thus, we parameterize the upper mantle as a layer with a constant V_s . In the crystalline crust and upper mantle, V_p is calculated from the V_s following the Brocher's Law (Brocher, 2005):

$$V_p = 0.9409 + 2.0947V_s - 0.8206V_s^2 + 0.2683V_s^3 - 0.0251V_s^4 \quad (10)$$

And the density is obtained from the V_p by following the empirical equation of Brocher (2005):

$$\rho = 1.6612V_p - 0.4721V_p^2 + 0.0671V_p^3 - 0.0043V_p^4 + 0.000106V_p^5 \quad (11)$$

Model parameters	Range	Reference
Sediment thickness (km)	0–10	
V_{SV} at the top of the sediment layer (km/s)	0–3.0	Bassin et al. (2000)
V_{SV} at the bottom of the sediment layer (km/s)	0–3.0	Bassin et al. (2000)
Sedimentary V_p/V_s	1.80–3.0	
Crystalline crustal thickness (km)	20–80	
4 B-spline coefficients for the crystalline crust (km/s)	3.1–4.4	Bassin et al. (2000)
V_s for the upper mantle (km/s)	4.0–5.4	Bassin et al. (2000)
3 uncertainties (σ)	10^{-4} – 10^{-1}	

Nine variables in total are used to determine the 1-D model velocity structure. Table 1 lists the sampling range of those parameters in our joint inversion.

4. Results

4.1. Phase Velocity Maps

Rayleigh wave phase velocity maps inverted from the Z-Z CCFs are plotted in Figure 6 at four selected periods of 4, 8, 12 and 15 s. Checkerboard tests (Figure S1) indicate that there are enough crossing raypaths

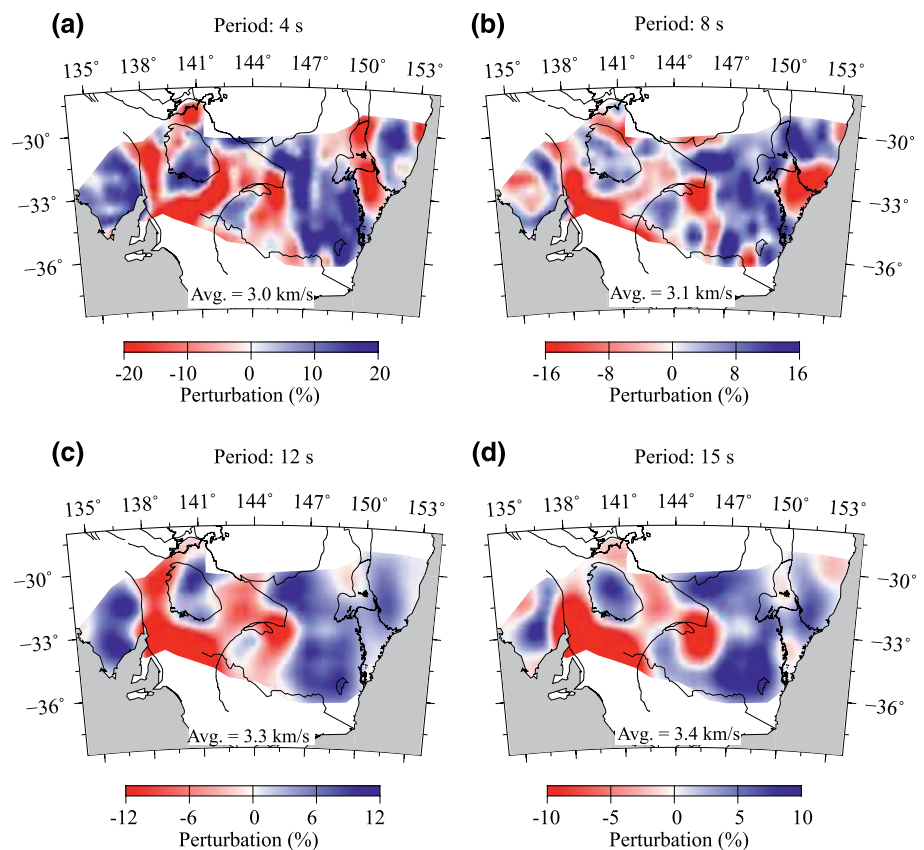


Figure 6. Rayleigh wave phase velocity maps at four periods of 4, 8, 12, and 15 s. Phase velocities are plotted as perturbations relative to the average at individual period. The average phase velocity at each period is indicated at the bottom of each panel for the corresponding period.

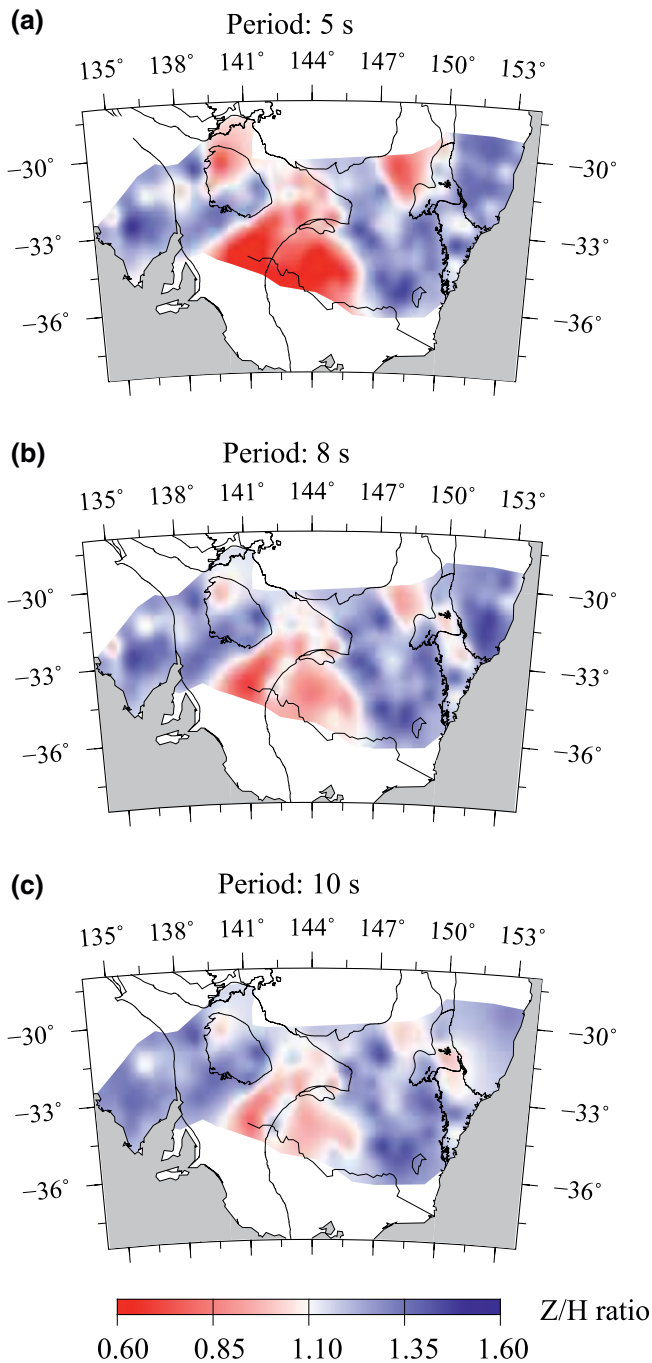


Figure 7. Rayleigh wave Z/H ratio maps at three periods of 5, 8 and 10 s.

to recover anomalies with a size of $1^\circ \times 1^\circ$. At 4 s, phase velocities show three main low-velocity zones. From west to east, the first low-velocity zone is located in the Adelaide Fold Belt between the Gawler Graton and Curnamona province. The second low-velocity zone is concentrated in the Murray Basin, and the third low-velocity zone is in the SGBB system. From the sensitivity kernel of 4 s Rayleigh wave phase velocity (Figure 5a), it can be seen that although the most sensitive depths of Rayleigh wave at 4 s period range from 2.0 to 7.0 km, the velocity structure above 1.0 km also affects the phase velocity, which can explain the low-velocity anomalies inside the Murray Basin and the SGBB. The low-velocity anomaly under the Adelaide Fold Belt is unlikely caused by the sediments and the possible reason for this low velocity will be discussed in the Discussion section. At 8 s, Rayleigh wave phase velocities show similar low- and high-velocity patterns with those of 4 s, except that there is an extra low-velocity zone appearing in the Gawler Craton. At 12 s and 15 s, Rayleigh wave phase velocities are mainly sensitive to the middle crust (Figure 5a). At these periods, one prominent feature is a low-velocity zone surrounding the Curnamona Province. Besides, there is another low-velocity zone concentrated in the Begargo Hill volcanic zone (red square labeled as BH in Figure 1b).

4.2. Rayleigh Wave Z/H Ratio

We plot Z/H ratio maps at 5, 8 and 10 s periods by interpolating the measurements from each station in Figure 7. Since the most sensitive depths of Z/H ratios at those periods are concentrated at the top few kilometers (Figure 5b), low Z/H ratio anomalies are related to sedimentary basins. The three Z/H ratio maps reveal very low Z/H ratios inside the Murray Basin, suggesting that the basin is filled with low-velocity unconsolidated sediments. The low Z/H ratios are difficult to be explained by crystalline crustal rocks at elevated temperature. Similarly, the SGBB system also stands out with low Z/H ratios. On average, the measured Z/H ratio at the SGBB is higher than that in the Murray Basin, suggesting the sediments in the SGBB system may be more consolidated than those in the Murray Basin (e.g., Boore & Toksoz, 1969; Chong et al., 2014). Interestingly, the northern Curnamona Province also exhibits low Z/H ratios, while the southern part of the Curnamona Province has relatively high Z/H ratios, suggesting that the two areas likely have different sedimentary history. In fact, the northern Curnamona is largely covered by Cenozoic sedimentation of the Lake Eyre Basin, while the southern Curnamona belongs to the remnant of a late Paleoproterozoic sedimentary basin infilled with the metamorphosed Willyama Supergroup (Armistead et al., 2018; Conr & Preiss, 2008). In general, with increasing periods the contrasts between the low and high Z/H ratios become smaller as the sensitivity depth ranges of longer period Z/H ratio extend to a greater depth (Figure 5b).

4.3. 3-D Vs Model

We first invert Rayleigh wave dispersion curve, Z/H ratios, and body waves for a 1-D Vs profile beneath each station following the joint inversion method described in Subsection 3.5. We show an example of the joint inversion at station CU08 (Figure 8). Figure 8 shows an example of the posterior density function of the inverted 1-D Vs at station CU08, which suggests that the model is well constrained by the three datasets. Overall, the observed phase velocities (Figure 8c) and Z/H ratios (Figure 8d) are well fitted by the inverted

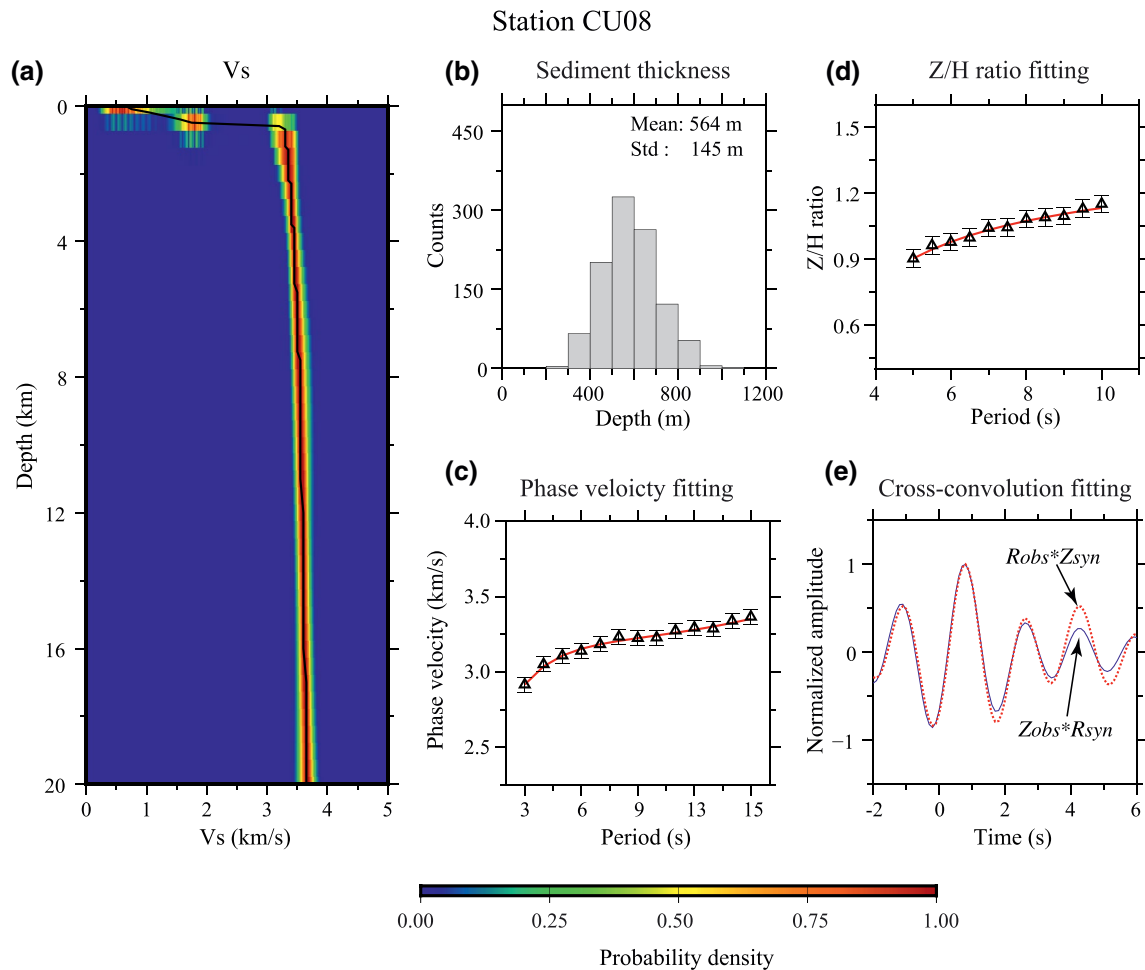


Figure 8. An example of joint inversion at station CU08. (a) Color map shows the posterior density function of the 1-D V_s with the black line representing the maximum probability model. (b) Histogram of sediment thickness estimated from 1,000 acceptable models. (c) Phase velocity fitting. Black triangles show the measured phase velocities and the red line represents the theoretical dispersion curve calculated from the maximum probability model. (d) Same as (b) except for Z/H ratio. (e) Cross-convolution fitting. The two cross convolutions between the observed and synthetic waveforms computed from the maximum probability model are shown in solid blue line ($Z_{obs} * R_{syn}$) and dotted red line ($R_{obs} * Z_{syn}$), respectively. Note the excellent match between the two convolutions.

V_s model. The zero-lag cross-correlation coefficient of the two cross-convolution functions is 0.98 (Figure 8e), suggesting that the teleseismic body wavefield is also well fitted by the model.

Then, we assemble all these 1-D V_s profiles and linearly interpolate them to build a 3-D V_s model that extends from surface down to 20 km (Figure 9). At shallow depths, like 0.4 km (Figure 9a), the most prominent features are distinct low-velocity zones associated with sedimentary basins. From west to east, the first pronounced low-velocity zone appears in the northern part of the Curnamona Province, which is associated with the Cenozoic Lake Eyre Basin that does not reach to the southern part of the Curnamona Province as mentioned in the above section. The second pronounced low-velocity zone is in the Murray Basin. The Murray Basin extends over a large area, containing a thin layer of Cenozoic sediments (200–400 m) with a maximum thickness of 600 m as suggested by Brown and Stephenson (1991). The third less pronounced low-velocity zone at this depth appears in the SGBB system, which separates the Lachlan and New England orogen. The average V_s at 0.4 km depth in the Murray Basin is 1.10 km/s, while the average V_s at that depth within SGBB system is 2.04 km/s.

At 1 km depth, the most pronounced features are still the low velocities associated with major sedimentary basins (Figure 9b). However, compared with velocity distributions at depth of 0.4 km, the low velocity zones at 1.00 km depth are only limited to several smaller areas, especially those low velocity zones beneath the Murray Basin, indicating that the thickness of the sedimentary deposits is less than 1.0 km in most parts of

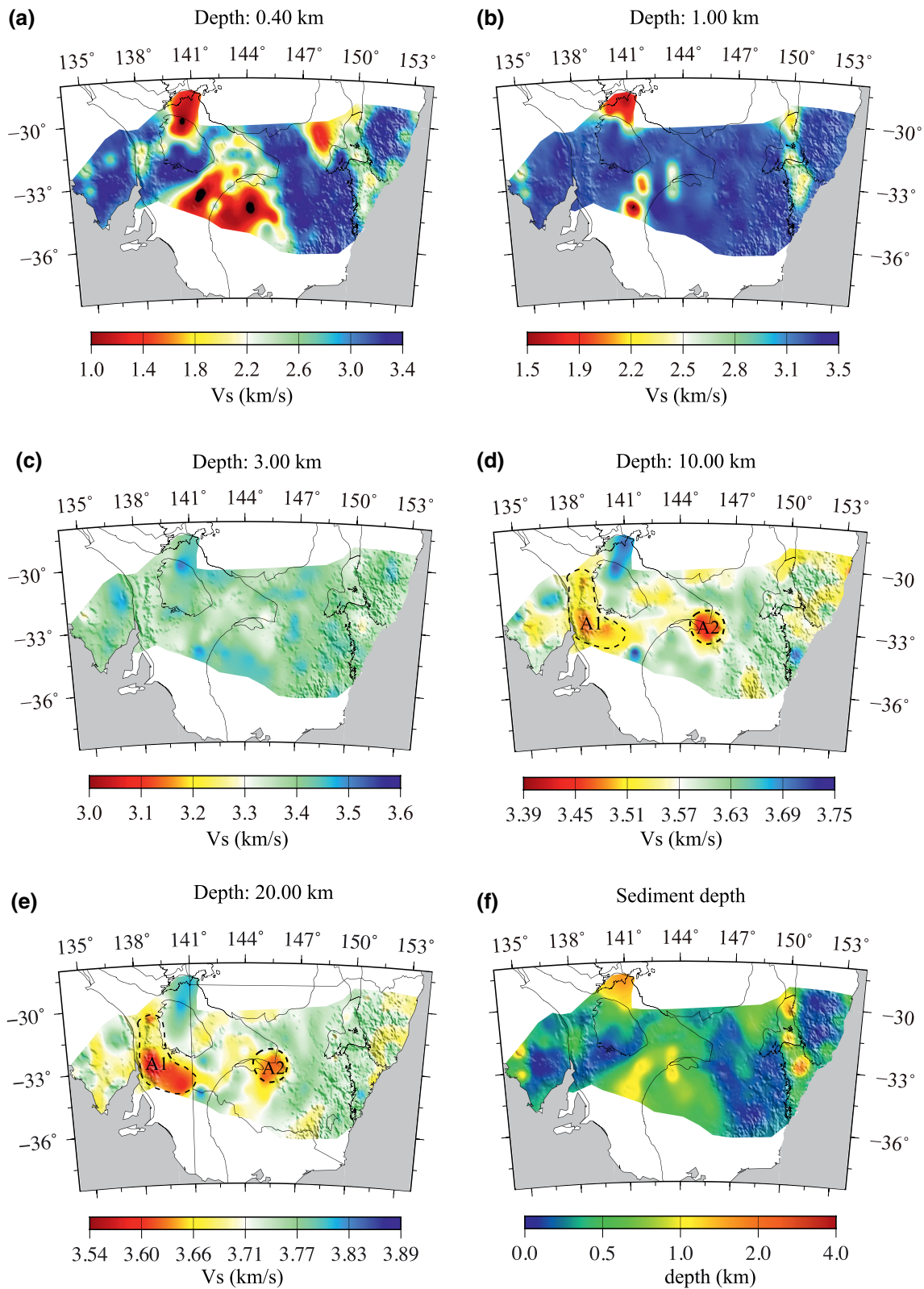


Figure 9. (a–e) V_s maps at five different depths of 0.4, 1.0, 3.0, 10.0, and 20 km. (f) Map of sediment depths. A1 and A2 outline two low-velocity zones in the mid-crust.

the Murray Basin. In the Murray Basin, there are a number of pre-Tertiary infra-basin concealed beneath the Quaternary sediments (Knights et al., 1995). Those infra-basins formed in the Late Paleozoic and appear to be aligned with the strike of the basement terrane and are associated with grabens and downwarps of the underlying crust (Arroucau et al., 2010). In general, we find a good spatial correlation between the low velocity zones within the Murray Basin and those pre-Tertiary infra-basins derived from borehole, gravity and magnetic data. The low-velocity anomalies beneath the SGBB are still as prominent as those at 0.4 km depth and extend to the depth of ~ 3.0 km (Figure 9c).

Because the longest period of Rayleigh wave phase velocity used is 15 s, we can reliably resolve the velocity structures at depths up to ~ 20 km. The velocity patterns of the upper crust from ~ 5 to 20 km are quite similar, and the velocity variations in the crystalline crust are much smaller than those in the sedimentary layers. In the upper crust, we observe two major low velocity anomalies whose locations are marked by black dash lines in Figures 9d and 9e. The first low velocity anomaly, denoted as A1, appears in the areas of the Adelaide Fold Belt to the west and south margin of the Curnamona province, which reaches to its maximum amplitude at ~ 20 km with a velocity reduction of $5 \pm 2\%$. As aforementioned, this low velocity zone is also observed by other tomography studies (e.g., Pilia et al., 2015; Saygin & Kennett, 2010). The second low velocity anomaly A2 is associated with a volcanic belt near the Begargo Hill Volcanic zone and is $\sim 4 \pm 2\%$ less than the mean velocity at depth of 10 km.

Based on our results, we plot the map of sedimentary thickness in Figure 9f. As seen from the figure, in most areas of the Murray Basin, the sediment depth is ~ 600 m with a maximum depth of 1,500 m. On average, the sediment depth in the Murray Basin is 713 m. In the SGBB, the average sediment depth is 600 m with a maximum depth of $\sim 3,000$ m.

5. Discussions

We have assumed a linearly increasing V_s within the sedimentary layer in order to reduce the number of model parameters. Numerical tests with more complicated sediment models suggest that the inverted model represents a good linear approximation of the input model (Figure S2a). In our inversion, we have employed empirical relationships in scaling V_s to V_p in sediment and crystalline crust and mantle instead of using a constant V_p/V_s ratio during the inversion. We also conducted numerical tests by using a constant V_p/V_s of 2.0 for the sediment and 1.732 for the crystalline crust and model. In general, the two scaling implementations have led to very similar results (Figure S2b).

Unlike previous studies (e.g., Li et al., 2016; Lin et al., 2014; Shen & Ritzwoller, 2016), we treat the uncertainties (σ_1 , σ_2 , and σ_3) of the three kinds of datasets as three unknowns, which are included in the joint inversion. The inverted uncertainties are 0.05 km/s, 0.03 and 0.04 for the phase velocity, Z/H ratio, and cross-convolution misfit function, respectively. These values are comparable to those measured by previous studies, such as Shen & Ritzwoller (2016) from the USArray data.

As mentioned previously, the posterior density functions of the inverted V_s at each station suggest that these models are well constrained. We also compute the average phase velocity residuals, average Z/H ratio residuals and the cross-convolution misfit function residuals across the study area, which are shown in Figures 3Sa–3Sc, respectively. The phase velocity residuals are generally less than 0.075 km/s (Figure S3a), and Z/H ratios are mostly in the range of 0.00–0.050 (Figure S3b), while the cross-convolution misfit is less than 7.5% (Figure S3c). Uncertainty in the inverted sediment thickness is mostly less than 300 m (Figure S3d).

5.1. Comparisons with Borehole Data

To evaluate the reliability of our 3-D model, especially the obtained thickness of sediments, we compare our V_s model with the borehole data, which have the ground-truth thickness of the sedimentary layer. We find four boreholes in the Sydney Basin region with their sites close to one of our seismic stations (Figure 10). As the four borehole sites are nearly aligned in a west-east running line connecting station E2E9 and station E2G2, that is, the gray lines shown in the inset of Figure 1a. We plot the comparisons between our models beneath three stations and the drilled sediment depths along that line. In Figure 10 we show the 1-D V_s model beneath five stations along the line, together with the locations of the four boreholes used

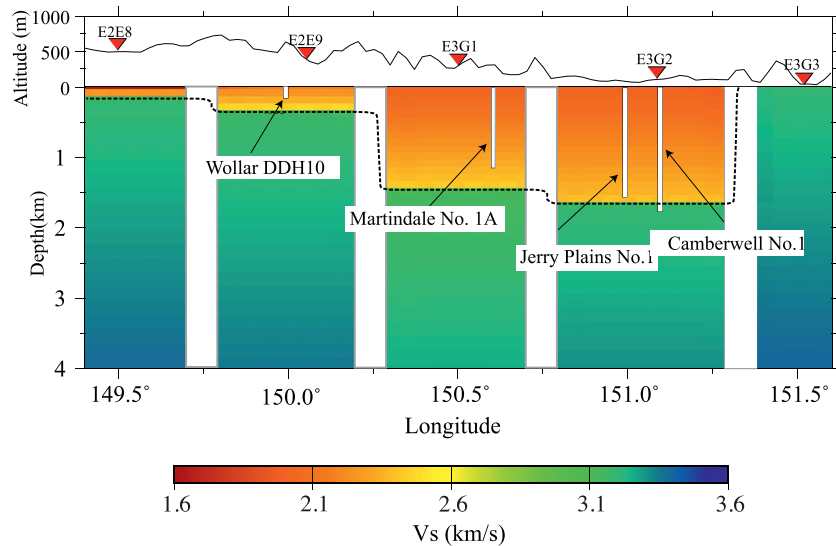


Figure 10. Vs transects along the profile delineated as the gray line in Figure 1a. The Vs columns represent the 1-D Vs models right beneath the corresponding stations as marked by the red inverse triangles. The dotted line marks the inverted sediment depths under the five stations. The four white vertical bars represent the four boreholes that drilled through the sedimentary layer. The names of the boreholes are indicated by the annotations. The ground-truth sediment depths from the four boreholes is represented by the bottom of the bars.

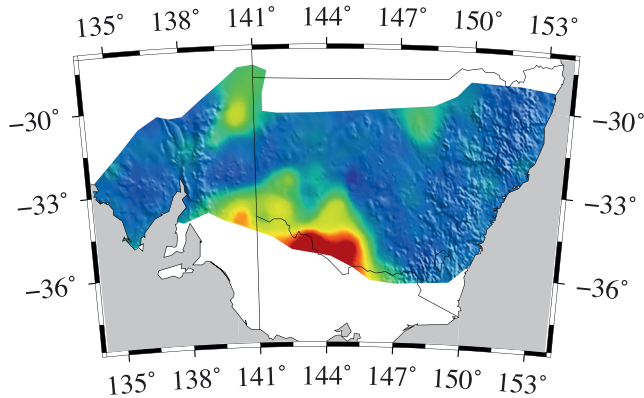
for verification. We are unable to obtain the velocity profiles of those boreholes but have the ground-truth sedimentary depths of the four borehole sites.

From west to east, the first borehole, named as the Wollar DDH10 and marked as the vertical white thin column, was 9.64 km away from station E2E9. The sedimentary depth from Wollar DDH1 is 149.0 m. The sedimentary depth beneath station E2E9 from our model is 350.0 ± 262.0 m. The second borehole named Martindale No. 1A is 11.16 km away from station E3G1, and the sedimentary thickness from the borehole is 1147.8 m, which is very close to the depth of 1450.0 ± 320.0 m beneath station E3G1 from our inversion. The third and fourth boreholes are both close to station E3G2 and their distances away from station E3G2 are 13.99 km and 7.89 km respectively. The corresponding sedimentary thicknesses from the two boreholes are 1533.4 m and 1818.8 m respectively, which are also close to the inverted sedimentary depth of 1650.0 ± 305.0 m beneath station E3G2. For these three stations, the average difference of the sedimentary depths between the borehole measurements and our inverted results is 197.1 m, which is reasonable given the fact that (1) the locations of seismic stations and the boreholes are not exactly the same; and (2) the thickness of sedimentary layer changes quickly laterally as shown by the large differences of sedimentary depths between the two close boreholes of Jerry Plains No. 1 and Camberwell No.1 (Figure 10). In order to better evaluate the reliability of our inverted results of sedimentary basins, we need to find seismic stations located at the exact same site as boreholes, which will be pursued in a future study if such kind of data are available.

5.2. Implications on Sedimentation Histories

As shown by the map of sedimentary thickness from our model in Figure 9f, the average sedimentary depth of the Murray Basin is 713 m; while, the sedimentary depths at most parts of the SGBB are thicker than 600 m with the deepest sedimentary depth reaching 3,000 m, much thicker than those in the Murray Basin. The Murray Basin is a low-lying, saucer-shaped intracratonic basin, containing flat-lying Tertiary sediments. Brown and Stephenson (1991) suggested that the Tertiary sediments of the Murray Basin consists of three major depositional sequences, including an early Paleocene-Eocene to early Oligocene sequence of Renmark Group, an Oligocene to middle Miocene marine sequence of Murray Group, and a late Miocene to Pliocene marine-fluvial sequence of Wunghnu Group (Brown & Stephenson, 1991). As these sediments are newly formed and still lack of gravity compaction, Vs of the sedimentary layer is very low with an average of 1.10 km/s at 400 m depth, suggesting sediments maybe not well compacted and cemented. The SGBB is

(a) Horizontal component of Rayleigh wave



(b) Love wave

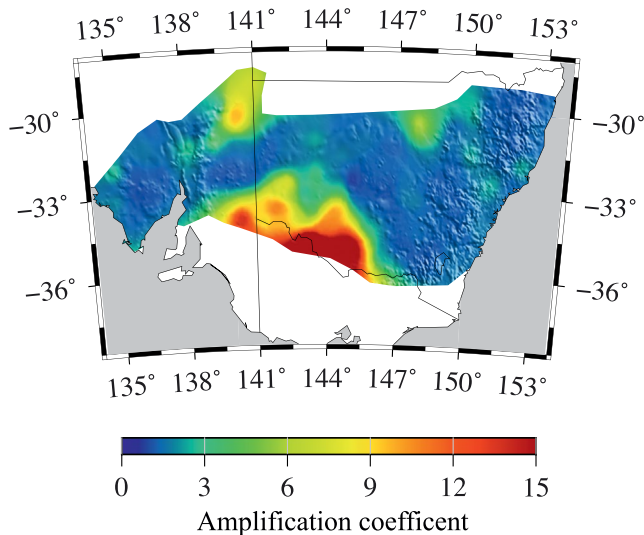


Figure 11. Seismic site amplification coefficient for Rayleigh wave horizontal component (a) and for Love wave (b) averaged in the frequency band of 0.2–0.5 Hz.

a Permian-Triassic basin with the ages of the main strata ranging from the later Carboniferous to Middle Triassic (Bembrick & Lonergan, 1976; Herbert, 1980). V_s at 400 m depth in the SGBB is 2.04 km/s, much higher than that in the Murray Basin, suggesting sediments inside the SGBB are well compacted and cemented.

As mentioned in the Introduction section, one of the main applications of our 3-D velocity model is that it allows us to calculate the site amplification coefficients of strong ground motion, which is fundamental to seismic hazard mitigation. To do so, we employ the semi-analytical method of Bowden and Tsai (2017), and calculate the average seismic site amplification coefficients for each station at the frequency band of 0.5–0.2 Hz. Figure 11 shows the amplification coefficient map of the study area by linearly interpolating the results at each station. As mentioned above, although the deepest sedimentary depth of the SGBB is greater than that in the Murray Basin, the Murray Basin contains more unconsolidated sediments than the SGBB. Hence, the Murray Basin is more vulnerable to seismic hazards. From the horizontal Rayleigh wave and Love wave site amplification maps (Figure 11) we can see that, in the Murray Basin, the amplification coefficients can be up to 13, indicating that this area is vulnerable to seismic hazards from earthquakes that happened in the surrounding regions, like those in the Flinders Ranges (denoted in Figure 1b), one of most seismically active zones in Australia (Setiawan, 2017).

5.3. Low Velocity Anomalies in the Upper Crust

Australia is one of the most stable continents in the world. However, Australia still experiences a lot of intraplate earthquakes. A large number of earthquakes in southeast Australia occur in the Adelaide Fold Belt, where earthquakes with magnitudes larger than 6.0 occurred in the past (Holford et al., 2011). In that region, Pilia et al. (2013) constructed a P-wave model of the upper and middle crust using 24 stations deployed within the Adelaide Fold Belt. According to their tomography results, there are two low P-wave velocity and low V_p/V_s ratio zones in the upper and middle crust of the Adelaide Fold Belt zone and they suggested that the low-velocity zones in the Adelaide Fold Belt delineate mechanically weak zones that correspond well with intraplate deformation in the Adelaide region. Heat flow study (Holford et al., 2011) in this region reveals that the average heat flow in the Adelaide Fold Belt is also very high and can reach up to $\sim 90 \text{ mWm}^{-2}$. However, based on the heat flow observations,

Holford et al. (2011) suggested that it is the thermal effects that weaken the crust of the Adelaide Fold Belt, leading to the concentration of high seismicity in the Adelaide Fold Belt. In our study, we observe low velocities in most parts of the Adelaide Fold Belt at the upper to middle crust depths, denoted as A1 in Figures 9d and 9e. We notice that this low-velocity area is also featured by high heat flow, therefore, A1 is likely caused by high temperature anomaly at the same depths. Alternatively, the low-velocity A1 anomaly could be compositional, such as granite that has low seismic velocity due to its high concentration of quartz mineral (Lowry & Perez-Gussinye 2014). The granitic composition also seems to be a reasonable explanation for the high seismicity and high deformation observed in this area as the presence of quartz generally makes granite mechanically weak (Burgmann & Dresen, 2008). Granite also has a relatively high concentration of radioactive elements (K, U, Th), which is consistent with the heat flow data.

We also observe another low-velocity zone, denoted as A2 in Figures 9d and 9e, in the upper to middle crust beneath the Begargo Hill volcanic zone within the Lachlan Orogen, where there are almost no seismic activities. In eastern Australia, several studies (Cohen et al., 2013; Davies et al., 2015) delineated a 2,000 km long

volcanic track, extending from the Fraser Island in Queensland to Cosgrove in Victoria. Davies et al. (2015) proposed that this volcanic train was formed as a result of the northward movement of the Australian continent over a mantle plume, which is currently located at the Bass Strait. As it is a hotspot track, the volcanic rocks progressively become younger from the north to the south of the volcanic chain. Along the volcanic chain, they found a strong correlation between the lithosphere depth and the magma composition on the surface. More specifically, according to their study, the magma from the plume erupted as standard basaltic volcanism in areas with lithosphere thickness less than 110 km; low-volume, leucitite-bearing volcanism appears in regions where lithosphere thickness is between 110 and 150 km. For regions with lithosphere thickness greater than 150 km, volcanic eruption ceases as it is hard for magma to break through the thick lithosphere. In the Begargo Hill volcanic zone, the lithosphere thickness is between 110 and 150 km (Davies et al., 2015) and the lavas erupted at around 18–15 Ma. The low velocity in the upper to middle crust based on our model is coincident with the site being a young volcanic area. A significant amount of magma was likely produced in the upper to middle crust under the Begargo Hill during the Miocene eruption, and the heated crust remains hot enough today to cause a ~4% reduction in S-wave velocity.

6. Conclusions

In this study, we build a 3-D upper crustal S-wave velocity model up to 20 km deep beneath southeastern Australia by jointly inverting Rayleigh wave phase velocity, Rayleigh wave ellipticity, and teleseismic P-coda waveforms. As Rayleigh wave ellipticity and teleseismic body wave have complementary sensitivities to sediment velocity and thickness, our 3-D Vs model has a good constraint on the sedimentary structures beneath the major basins.

Our model shows that the average sediment depth of the Murray Basin is 713 m with a maximum depth of 1,500 m and the average depth of the SGBB is 600 m with a maximum depth of ~3,000 m. To evaluate the accuracy of the sediment depths of our model, we compare them with ground-truth sediment depths from four boreholes. On average, the differences between them are less than 200 m, which is reasonable given the fact that the locations of the corresponding stations and the boreholes are apart from each other with an average distance of 10.67 km. In addition, our model reveals that the Vs of sedimentary layers in the Murray Basin is on average less than that in the SGBB, suggesting that the sediments in the Murray Basin are less consolidated than those in the SGBB. The unconsolidated sediments make the Murray Basin more vulnerable to seismic hazards according to the seismic amplification map calculated based on our model.

In the upper to middle crustal depths, our model resolves two low-velocity zones: one beneath the Adelaide Fold Belt and the other beneath the Begargo Hill volcanic zone. The low-velocity zone beneath the Adelaide Fold Belt is coincident with abnormally high heat flows in this region, suggesting that thermal weakening may be the main reason leading to the concentration of intraplate seismic activities in this area. The low-velocity zone beneath the Begargo Hill volcanic zone may suggest that there still exists magma in the upper to middle crust or the temperature there is still high after the latest eruption.

Data Availability Statement

This is contribution 1549 from the ARC Centre of Excellence for Core to Crust Fluid Systems (<http://www.cafs.mq.edu.au>) and 1414 in the GEMOC Key Centre (<http://www.gemoc.mq.edu.au>).

References

- Afonso, J. C., Fullea, J., Griffin, W. L., Yang, Y., Jones, A. G., Connolly, J. A. D., & O'Reilly, S. Y. (2013). 3-D multiobservable probabilistic inversion for the compositional and thermal structure of the lithosphere and upper mantle. I: A priori petrological information and geophysical observables. *Journal of Geophysical Research: Solid Earth*, 118(5), 2586–2617. <https://doi.org/10.1002/jgrb.50124>
- Armistead, S. E., Betts, P. G., Ailleres, L., Armit, R. J., & Williams, H. A. (2018). Cu-Au mineralization in the Curnamona Province, South Australia: A hybrid stratiform genetic model for Mesoproterozoic IOCG systems in Australia. *Ore Geology Reviews*, 94, 104–117. <https://doi.org/10.1016/j.oregeorev.2018.01.024>
- Arroucau, P., Rawlinson, N., & Sambridge, M. (2010). New insight into Cainozoic sedimentary basins and Palaeozoic suture zones in southeast Australia from ambient noise surface wave tomography. *Geophysical Research Letters*, 37, L07303. <https://doi.org/10.1029/2009GL041974>

Acknowledgments

We used seven subarrays (CU, EAL1, EAL2, EAL3, GW, SEAL1, and SEAL2) of the WOMBAT Seismic Array, which are managed by the Research School of Earth Sciences (RES), Australian National University (ANU) (https://doi.org/10.7914/SN/1F_2009 and https://doi.org/10.7914/7T_2007). The cross-correlations and teleseismic waveforms used in this study as well as the phase velocity and Z/H ratio measurements are archived at the online repository <https://figshare.com>. We would like to thank the members of RSES, ANU who have deployed the extensive sets of portable seismic recorders across the Australian continent. We also thank the Editor (Dr. Michael Bostock), Associate Editor (Dr. Fan-Chi Lin), Dr. Nicholas Rawlinson, and another anonymous reviewer for their constructive and thoughtful comments and suggestions, which have significantly improved the quality of this paper. This work was jointly supported by the National Key Research and Development Program of China (No. 2017YFC1500303) and the National Natural Science Foundation of China (No. 41630209). Yingjie Yang is supported by an Australian Research Council Discovery Grant (DP190102940) and Future Fellowship (FT130101220).

- Bao, Y., & Niu, F. (2017). Constraining sedimentary structure using frequency dependent P-wave particle motion: a case study of the Songliao Basin in NE China. *Journal of Geophysical Research: Solid Earth*, 122, 9083–9094. <https://doi.org/10.1002/2017JB014721>
- Bassin, C., Laske, G., & Masters, G. (2000). The current limits of resolution for surface wave tomography in North America. *EOS Transactions AGU*, 81, F897.
- Bembrick, C. S., & Lonergan, A. D. (1976). Sydney Basin. In R. B. Leslie, B. Evans, & C. L. Knight (Eds.), *Economic geology of Australia and Papua New Guinea 3, petroleum* (pp. 426–438). Melbourne, Australia: Australian Institute of Mining and Metallurgy.
- Bensen, G. D., Ritzwoller, M. H., Barmin, M. P., Levshin, A. L., Lin, F., Moschetti, M. P., et al. (2007). Processing seismic ambient noise data to obtain reliable broad-band surface wave dispersion measurements. *Geophysical Journal International*, 169(3), 1239–1260. <https://doi.org/10.1111/j.1365-246X.2007.03374.x>
- Bodin, T., Yuan, H., & Romanowicz, B. (2014). Inversion of receiver functions without deconvolution—Application to the Indian craton. *Geophysical Journal International*, 196, 1025–1033. <https://doi.org/10.1093/gji/ggt431>
- Boore, D. M., & Toksoz, M. N. (1969). Rayleigh wave particle motion and crustal structure. *Bulletin of the Seismological Society of America*, 59(1), 331–346.
- Bowden, D. C., Tsai, V. C., & Lin, F. C. (2015). Site amplification, attenuation, and scattering from noise correlation amplitudes across a dense array in Long Beach, CA. *Geophysical Research Letters*, 42, 1360–1367. <https://doi.org/10.1002/2014GL062662>
- Brocher, T. M. (2005). Empirical relations between elastic wavespeeds and density in the Earth's crust. *Bulletin of the Seismological Society of America*, 95(6), 2081–2092.
- Brown, C. M., & Stephenson, A. E. (1991). Geology of the Murray Basin, Southeastern Australia. Bur. Miner. Resour. (Vol. 235), Australian Government Publishing Service: Canberra.
- Burgmann, R., & Dresen, G. (1991). Rheology of the lower crust and upper mantle: Evidence from rock mechanics, geodesy, and field observations. *Annual Review of Earth and Planetary Sciences*, 36(1), 531–567. <https://doi.org/10.1146/annurev.earth.36.031207.124326>
- Castagna, J. P., Batzle, M. L., & Eastwood, R. L. (1985). Relationships between compressional-wave and shear-wave velocities in clastic silicate rocks. *Geophysics*, 50(4), 571–581.
- Chong, J., Ni, S., & Zhao, L. (2014). Joint inversion of crustal structure with the Rayleigh wave phase velocity dispersion and the ZH ratio. *Pure and Applied Geophysics*, 172, 2585–2600. <https://doi.org/10.1007/s00024-014-0902-z>
- Cohen, B. E., Knesel, K. M., Vasconcelos, P. M., Thiede, D. S., & Hergt, J. M. (2008). ⁴⁰Ar/³⁹Ar constraints on the timing and origin of Miocene leucite volcanism in southeastern Australia. *Australian Journal of Earth Sciences*, 55(3), 407–418. <https://doi.org/10.1080/08120090701769514>
- Conor, C. H. H., & Preiss, W. V. (2008). Understanding the 1720–1640 Ma Paleoproterozoic Willyama Supergroup, Curnamona province, southeastern Australia: implications for tectonics, basin evolution and ore genesis. *Precambrian Research*, 166, 297–317. <https://doi.org/10.1016/j.precamres.2007.08.020>
- Danis, C. (2012). Sydney-Gunnedah-Bowen Basin deep 3D structure. *Exploration Geophysics*, 43(1), 26–35. <https://doi.org/10.1071/EG11043>
- Danis, C., O'Neill, C., Lackie, M., Twigg, L., & Danis, A. (2011). Deep 3D structure of the Sydney Basin using gravity modelling. *Australian Journal of Earth Sciences*, 58(5), 517–542. <https://doi.org/10.1080/08120099.2011.565802>
- Davies, D. R., Rawlinson, N., Iaffaldano, G., & Campbell (2015). Lithospheric controls on magma composition along Earth's longest continental hotspot track. *Nature*, 525, 511–514. <https://doi.org/10.1038/nature14903>
- Denham, D. (1992). Earthquake attack in the Sydney Basin: what is the risk? *Exploration Geophysics*, 23(4), 579–587. <https://doi.org/10.1071/EG992579>
- Dziewonski, A. M., & Anderson, D. L. (1981). Preliminary reference Earth model. *Physics of the Earth and Planetary Interiors*, 25(4), 297–356. [https://doi.org/10.1016/0031-9201\(81\)90046-7](https://doi.org/10.1016/0031-9201(81)90046-7)
- Dziewonski, A. M., Bloch, S., & Landisman, M. (1969). A technique for the analysis of transient seismic signals. *Bulletin of the Seismological Society of America*, 59, 427–444.
- Foster, D. A., & Gray, D. R. (2000). Evolution and structure of the Lachlan fold belt (orogen) of eastern Australia. *Annual Review of Earth and Planetary Sciences*, 28, 47–80.
- Gardner, G. H. F., Gardner, L. W., & Gregory, A. R. (1974). Formation velocity and density—The diagnostic basis for stratigraphic traps. *Geophysics*, 39(6), 770–780.
- Glen, R. A. (2013). Refining accretionary orogen models for the Tasmanides of eastern Australia. *Australian Journal of Earth Sciences*, 60(3), 315–370. <https://doi.org/10.1080/08120099.2013.772537>
- Hand, M., Reid, A., & Jagodzinski, L. (2007). Tectonic framework and evolution of the Gawler Craton, Southern Australia. *Economic Geology*, 102(8), 1377–1395. <https://doi.org/10.2113/gsecongeo.102.8.1377>
- Haskell, N. A. (1962). Crustal reflection of plane P and SV waves. *Journal of Geophysical Research*, 67(12), 4751–4768. <https://doi.org/10.1029/JZ067i012p04751>
- Herbert, C. (1980). Depositional development of the Sydney Basin. *Geological Survey of New South Wales Bulletin*, 26, 10–53.
- Herrin, E. E., & Goforth, T. T. (1977). Phase-matched filters: application to the study of Rayleigh Waves. *Bulletin of the Seismological Society of America*, 67, 1259–1275.
- Herrmann, R. B. (2013). Computer programs in seismology: An evolving tool for instruction and research. *Seismological Research Letters*, 84, 1081–1088. <https://doi.org/10.1785/0220110096>
- Holford, S. P., Hillis, R. R., Hand, M., & Sandiford, M. (2011). Thermal weakening localizes intraplate deformation along the southern Australian continental margin. *Earth and Planetary Science Letters*, 305, 207–214. <https://doi.org/10.1016/j.epsl.2011.02.056>
- Jenkins, R. J. F., & Sandiford, M. (1992). Observations on the tectonic evolution of the southern Adelaide fold belt. *Tectonophysics*, 214, 27–36. [https://doi.org/10.1016/0040-1951\(92\)90188-C](https://doi.org/10.1016/0040-1951(92)90188-C)
- Jessop, K., Daczko, N. R., & Piazzolo, S. (2019). Tectonic cycles of the new England orogen, eastern Australia: A review. *Australian Journal of Earth Sciences*, 66, 1–38. <https://doi.org/10.1080/08120099.2018.1548378>
- Jiang, C., Yang, Y., Rawlinson, N., & Griffin, W. L. (2016). Crustal structure of the newer volcanics province, SE Australia, from ambient noise tomography. *Tectonophysics*, 683, 382–392. <https://doi.org/10.1016/j.tecto.2016.06.033>
- Kennett, B. L. N., Sambridge, M. S., & Williamson, P. R. (1988). Subspace methods for large scale inverse problems involving multiple parameter classes. *Geophysical Journal International*, 94, 237–247. <https://doi.org/10.1111/j.1365-246X.1988.tb05898.x>
- Kennett, B. L. N., Saygin, E., Fomin, T., & Blewett, R. (2016). *Deep crustal seismic reflection profiling: Australia, 1978-2015*. Canberra, Australia: ANU Press and Geoscience Australia.
- Knight, L. A. (1995). *A preliminary appraisal of the pre-tertiary infrabasins beneath the Murray Basin, northwestern Victoria, VIMP Report 16* (p. 136). Geological Survey of Victoria.

- Krassay, A. A., Korsch, R. J., & Drummond, B. J. (2009). Meandarra Gravity Ridge: symmetry elements of the gravity anomaly and its relationship to the Bowen-Gunnedah-Sydney basin system. *Australian Journal of Earth Sciences*, 56, 355–379. <https://doi.org/10.1080/08120090802698695>
- Levshin, A. L., & Ritzwoller, M. H. (2001). Automated detection, extraction, and measurement of regional surface waves. In *Monitoring the Comprehensive Nuclear-Test-Ban Treaty: Surface Waves*. (pp. 1531–1545) Basel: Birkhäuser.
- Li, G., Chen, H., Niu, F., Guo, Z., Yang, Y., & Xie, J. (2016). Measurement of Rayleigh wave ellipticity and its application to the joint inversion of high-resolution S wave velocity structure beneath northeast China. *Journal of Geophysical Research: Solid Earth*, 121, 864–880. <https://doi.org/10.1002/2015JB01245>
- Li, G., Niu, F., Yang, Y., & Tao, K. (2019). Joint inversion of surface wave phase velocity, particle motion and teleseismic body wave data for sedimentary structures. *Geophysical Research Letters*, 46, 6469–6478. <https://doi.org/10.1029/2019GL082746>
- Li, G., Niu, F., Yang, Y., & Xie, J. (2018). An investigation of time-frequency domain phase weighted stacking and its application to phase-velocity extraction from ambient noise's empirical Green's functions. *Geophysical Journal International*, 212, 1143–1156. <https://doi.org/10.1093/gji/ggx448>
- Lin, F.-C., Schmandt, B., & Tsai, V. C. (2012). Joint inversion of Rayleigh wave phase velocity and ellipticity using USArray: Constraining velocity and density structure in the upper crust. *Geophysical Research Letters*, 39, L12303. <https://doi.org/10.1029/2012GL052196>
- Lin, F. C., Tsai, V. C., & Schmandt, B. (2014). 3-D crustal structure of the western United States: application of Rayleigh-wave ellipticity extracted from noise cross-correlations. *Geophysical Journal International*, 198(2), 656–670. <https://doi.org/10.1093/gji/ggu160>
- Lowry, A. R., & Perez-Gussinye, M. (2014). The role of crustal quartz in controlling cordilleran deformation. *Nature*, 471(7338), 353–357. <https://doi.org/10.1038/nature09912>
- Menke, W., & Levin, V. (2003). The cross-convolution method for interpreting SKS splitting observations, with application to one and two-layer anisotropic earth models. *Geophysical Journal International*, 154(2), 379–392. <https://doi.org/10.1046/j.1365-246X.2003.01937.x>
- Miller, J. M. L., Phillips, D., Wilson, C. J. L., & Dugdale, L. J. (2005). Evolution of a reworked orogenic zone: The boundary between the Delamerian and Lachlan fold belts, southeastern Australia. *Australian Journal of Earth Sciences*, 52(6), 921–940. <https://doi.org/10.1080/08120090500304265>
- Payne, J. L., Hand, M., Barovich, K. M., & Wade, B. P. (2008). Temporal constraints on the timing of high-grade metamorphism in the northern Gawler Craton: implications for assembly of the Australian Proterozoic. *Australian Journal of Earth Sciences*, 55(5), 623–640. <https://doi.org/10.1080/08120090801982595>
- Pilia, S., Rawlinson, N., Cayley, R., Bodin, T., Musgrave, R., Reading, A. M., et al. (2015). Evidence of micro-continent entrainment during crustal accretion. *Scientific Reports*, 5, 8218. <https://doi.org/10.1038/srep08218>
- Pilia, S., Rawlinson, N., Direen, N. G., Cummins, P. R., & Balfour, N. (2013). Structural controls on localized intraplate deformation and seismicity in Southern Australia: Insights from local earthquake tomography of the Flinders Ranges. *Journal of Geophysical Research: Solid Earth*, 118, 2176–2190. <https://doi.org/10.1002/jgrb.50168>
- Rawlinson, N., Pilia, S., Young, M., Salmon, M., & Yang, Y. (2016). Crust and upper mantle structure beneath southeast Australia from ambient noise and teleseismic tomography. *Tectonophysics*, 689, 143–156. <https://doi.org/10.1016/j.tecto.2015.11.034>
- Rawlinson, N., & Sambridge, M. (2004a). Multiple reflection and transmission phases in complex layered media using a multistage fast marching method. *Geophysics*, 69, 1338–1350. <https://doi.org/10.1190/1.1801950>
- Rawlinson, N., & Sambridge, M. (2004b). Wavefront evolution in strongly heterogeneous layered media using the fast marching method. *Geophysical Journal International*, 156, 631–647. <https://doi.org/10.1111/j.1365-246X.2004.02153.x>
- Saygin, E., & Kennett, B. L. N. (2010). Ambient seismic noise tomography of Australian continent. *Tectonophysics*, 481, 116–125. <https://doi.org/10.1016/j.tecto.2008.11.013>
- Setiawan, B. (2017). Seismic hazard analysis of the Adelaide region, South Australia. *American Institute of Physics Conference Proceedings*, 1857, 1–7. <https://doi.org/10.1063/1.498707>
- Shen, W., & Ritzwoller, M. H. (2016). Crustal and uppermost mantle structure beneath the United States. *Journal of Geophysical Research: Solid Earth*, 121, 4306–4342. <https://doi.org/10.1002/2016JB01288>
- Thomson, W. T. (1950). Transmission of elastic waves through a stratified solid medium. *Journal of Applied Physics*, 21(2), 89–93. <https://doi.org/10.1063/1.1699629>
- Wade, C. E., Reid, A. J., Wingate, M., Jagodzinski, E. A., & Barovich, K. (2012). Geochemistry and geochronology of the c. 1585 Ma Benagerie Volcanic Suite, southern Australia: Relationship to the Gawler Range Volcanics and implications for the petrogenesis of a Mesoproterozoic silicic large igneous province. *Precambrian Research*, 51, 206–207. <https://doi.org/10.1016/j.precamres.2012.02.020>
- Wingate, M., Campbell, I. H., Compston, W., & Gibson, G. M. (1998). Ion microprobe U–Pb ages for Neoproterozoic basaltic magmatism in south-central Australia and implications for the breakup of Rodinia. *Precambrian Research*, 87, 135–159. [https://doi.org/10.1016/S0301-9268\(97\)00072-7](https://doi.org/10.1016/S0301-9268(97)00072-7)
- Yang, C., & Niu, F. (2019). Sedimentary structure of the Bohai Bay Basin revealed by frequency dependent P-wave particle motion. *Geodesy and Geodynamics*, 10, 372–381. <https://doi.org/10.1016/j.geog.2018.04.007>
- Young, M. K., Cayley, R. A., McLean, M. A., Rawlinson, N., Arroucau, P., & Salmon, M. (2013). Crustal structure of the east Gondwana margin in southeast Australia revealed by transdimensional ambient seismic noise tomography. *Geophysical Research Letters*, 40, 4266–4271. <https://doi.org/10.1002/grl.50878>